# ADVANCED MATERIALS

## Supporting Information

# Spin-Selective Full-Dimensional Manipulation of Optical Waves with Chiral Mirror

*Zhancheng Li, Wenwei Liu, Hua Cheng,\* Duk-Yong Choi, Shuqi Chen,\* and Jianguo Tian*

# Supporting Information

**Spin-selective full-dimensional manipulation of optical waves with chiral mirror**

Zhancheng Li, Wenwei Liu, Hua Cheng,* Duk-Yong Choi, Shuqi Chen,* and Jianguo Tian

Dr. Z. Li, Dr. W. Liu, Prof. H. Cheng, Prof. S. Chen, Prof. J. Tian
The Key Laboratory of Weak Light Nonlinear Photonics, Ministry of Education, School of Physics and TEDA Institute of Applied Physics, Renewable Energy Conversion and Storage Center, Nankai University, Tianjin 300071, China
E-mail: hcheng@nankai.edu.cn; schen@nankai.edu.cn
Prof. S. Chen
The Collaborative Innovation Center of Extreme Optics, Shanxi University, Taiyuan, Shanxi 030006, China
The Collaborative Innovation Center of Light Manipulations and Applications, Shandong Normal University, Jinan 250358, China
Prof. D.-Y. Choi
Laser Physics Centre, Research School of Physics, Australian National University, Canberra, ACT 2601, Australia
College of Information Science and Technology, Jinan University, Guangzhou 510632, China

**This file includes:**

*Figure S1*: The analysis for the wide-angle optical response of the enantiomorph A.

*Figure S2*: The influence of the structural parameter variation of the enantiomorph A on its spin-selective optical response.

*Figure S3*: The quantitative analysis of the enhanced spin-selective reflection in the proposed chiral mirrors

*Figure S4*: The analysis on the physical mechanisms for the spin-selective amplitude manipulation with the designed chiral mirrors.

*Figure S5*: The analysis on the physical mechanisms for the wavelength-selective amplitude manipulation with the designed chiral mirrors.

*Figure S6*: Spin-selective anomalous wave generation with the designed gradient chiral mirrors.

*Figure S7*: Schematic of the spin-encoded imaging with the designed chiral mirrors.

*Figure S8*: Schematic of the spin- and wavelength-encoded imaging with the designed chiral mirrors.

*Figure S9*: The experimental setup for spectra measurement and optical imaging.

**Section 1. The optical response of the chiral mirror in wide angle**

To validate the wide-angle optical response of the designed chiral mirrors, we simulated the variation of the modular square $r_{ij} = |R_{ij}|^2$ of the reflection coefficients for the enantiomorph A with the changing of the incident angle, as shown in **Figure S1**. The simulated results indicate that the spin-selective optical responses of the proposed chiral mirrors remain unchanged when the incident angle is below to 30 degrees.
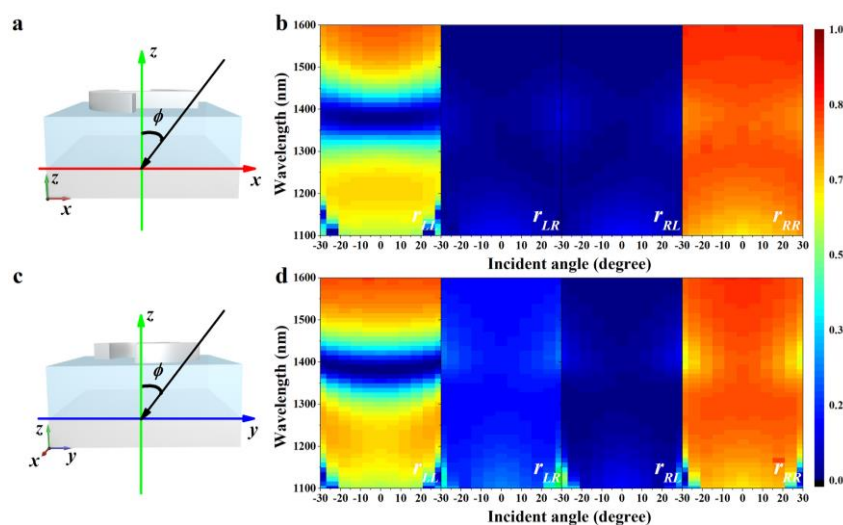


**Figure S1.** The analysis for the wide-angle optical response of the enantiomorph A. (a) Schematic of the oblique illuminating condition in *x-z* plane and (b) Simulated results of the variation of the modular square $r_{ij} = |R_{ij}|^2$ of the reflection coefficients for the enantiomorph A with the changing of the incident angle. (c) Schematic of the oblique illuminating condition in *y-z* plane and (d) Simulated results of the variation of the modular square of the reflection coefficients for the enantiomorph A with the changing of the incident angle.

**Section 2. The influence of the structural parameter variation on the optical response of the designed chiral mirrors**

To show the influence of the structural parameter variation on the optical responses of the designed chiral mirrors, we analyze the influence of the structural parameters ($P$, $w$, $r_1$, $r_2$, $t_1$ and $t_2$) variation on the modular square $r_{LL}$ and $r_{RR}$ of the reflection coefficients for the enantiomorph A, as shown in **Figure S2**. The simulated results indicate that the optical response of the enantiomorph A remains stable with a finite shift of the operation wavelength when these structural parameters varies in a certain range. Moreover, the results also show that the variation of $r_2$ results in a larger shift of the operation wavelength when compared with other structural parameters, the related discussion on the underlying physics can be found in section 4.
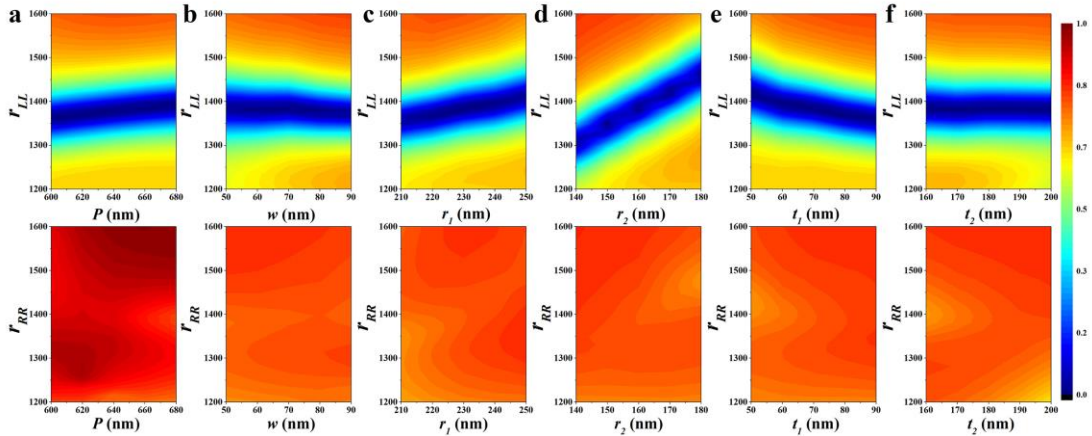


**Figure S2.** The influence of the structural parameter variation of the enantiomorph A on its spin-selective optical response. The results are obtained with structural variables α equals to 45 degrees, β equals to 80 degrees and $\theta$ equals to 0 degree. Simulated results of $r_{LL}$ and $r_{RR}$ for the enantiomorph A with (a) different $P$, (b) different $w$, (c) different $r_1$, (d) different $r_2$, (e) different $t_1$, (f) different $t_2$.

**Section 3. The quantitative analysis of the enhanced spin-selective reflection in the proposed chiral mirrors**

The proposed chiral mirrors have a metal-insulator-metal configuration. The upper aluminum nanostructures and the bottom aluminum layer constitute a Fabry-Pérot-like cavity, resulting in the multiple reflections of optical waves, which will significantly enhance the interaction between the nanostructures and the incident waves. Thus, a significant change of the distance between the aluminum nanostructures and the bottom aluminum layer will remarkably affect the resonance strength of the aluminum nanostructures. We utilized the matrix theory of multilayer optics and the multiple reflections and interference model to make a further quantitative analysis. **Figure S3**a shows the schematic of the multiple reflections and interference model for the designed chiral mirrors. For a planar interface between two media $i$ and $j$ (whether with or without a nano structures), the forward and backward propagating waves can be related by utilizing a 4×4 wave-transfer Matrix $\mathbf{M}_{ji}$ while a 4×4 propagation matrix $\mathbf{P}_i$ can be used for a homogeneous medium $i$. The forward and backward propagating waves at the two ends of a multilayered medium can be related by the overall wave-transfer matrix $\mathbf{M}$ of the multilayered medium that can be treated as the matrix product of each part: $\mathbf{M}=\mathbf{M}_n\cdots\mathbf{M}_2\mathbf{M}_1$, where the element $1,2,\ldots,N$ are numbered along the wave propagating direction. For the proposed chiral mirrors, the overall wave-transfer matrix $\mathbf{M}$ can be expressed as: $\mathbf{M}=\mathbf{M}_{cb}\mathbf{P}_b\mathbf{M}_{ba}$. We simulated the coefficients of the scattering matrix $\mathbf{S}_{ji}$ of each interface and calculated the corresponding wave-transfer matrix $\mathbf{M}_{ji}$. Then, we calculated the overall wave-transfer matrix $\mathbf{M}$ and retrieved the coefficients of the overall scattering matrix $\mathbf{S}$. Finally, the reflection intensities were calculated. Figures S3b,c show the simulated and calculated modular square $r_{ij} = |R_{ij}|^2$ of the reflection coefficients for the enantiomorph A with the changing of the thickness of the SiO$_2$ spacer layer, respectively. They are in good

4

agreement with each other. The enhancement of the spin-selective reflection in the designed chiral mirrors is attributed to the multiple reflections and interference of optical waves. According to the principle of the multiple reflections of optical waves in a Fabry-Pérot-like cavity, the interaction between the nanostructures and the optical waves can be enhanced when the equivalent distance between the nanostructures and the bottom aluminum layer is close to $(2n+1)\times\lambda/4$ (for example, $t_2 = 160$ to $200$ nm, see Figure S2f), where $\lambda$ is the operation wavelength, while the interaction between the nanostructures and the optical waves can be neglected when the equivalent distance between the nanostructures and the bottom aluminum layer is close to $(n+1)\times\lambda/2$ (for example, $t_2 = 420$ nm).
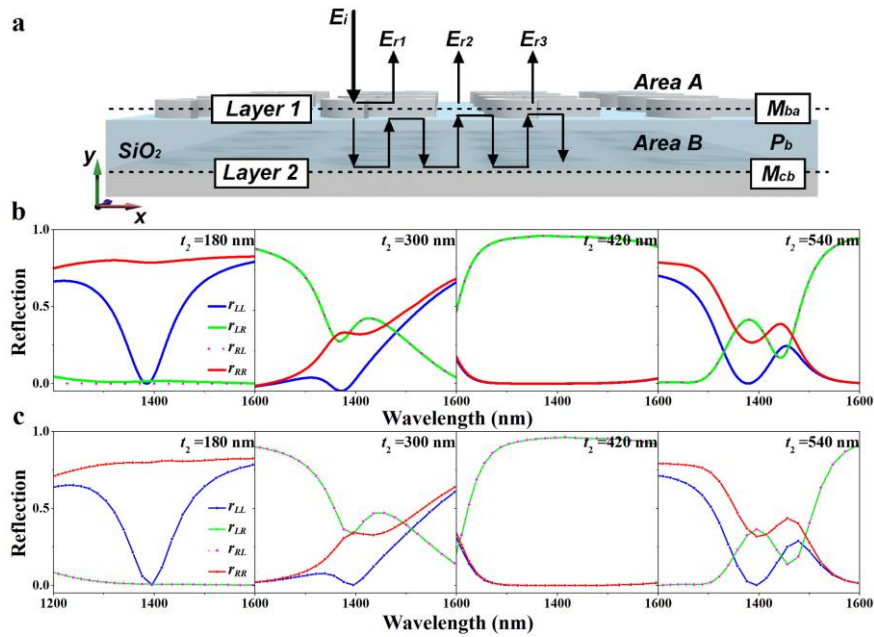


**Figure S3.** The Fabry-Pérot-like cavity of the proposed chiral mirrors and the functionality of spacer layer. (a) Schematic of the multiple reflections and interference model in the designed chiral mirrors. (b) Simulated and (c) Calculated modular square $r_{ij} = |R_{ij}|^2$ of the reflection coefficients for the enantiomorph A with the changing of the thickness $t_2$ of the SiO$_2$ spacer layer.

## Section 4. The analysis on the physical mechanisms of the designed chiral mirror for full-dimensional manipulation of optical waves

According to the qualitative and quantitative analysis in Figure 3, we obtained that the spin-selective reflection in the proposed chiral mirrors is ascribed to the generation of a pair of antiparallel currents within the nanostructures. The excited antiparallel currents within the nanostructures can be related to two electric dipoles with phase delay of $\pi$. Thus, the proposed structure can be equivalent to the optical nanoantenna whose second-order resonance has been excited. The excitation of the second-order resonance in the proposed structure is attributed to the symmetry breaking of the nanostructure by adding the short arc structure. And, according to Equation 1, the length of the short arc is directly associated with the efficiency of the spin-selective reflection in the proposed chiral mirrors. Therefore, we can manipulate the amplitude of the spin-selective reflection by controlling the length of the short arc structure (angle $\alpha$). To quantitative reveal the relationship between the angle $\alpha$ and the optical response of the chiral mirror, we analyzed the optical response of the enantiomorph A with different structural variable $\alpha$, as shown in **Figure S4**. As shown in Figure S4a, when $\alpha$ decrease to 25 degrees, the power loss density is dramatically declined, resulting in the increase of $r_{LL}$, which can be ascribed to the weaken of the excitation of the magnetic dipole along $z$-axis and the enhancement of the excitation of the electric dipole along $x$-axis (Figure S4i,m). Moreover, as shown in Figure S4e–h, $r_{LL}$ can be effectively manipulated by changing angle $\alpha$, which get minimum value when $\alpha$ equal to 45 degrees. Despite that the operation wavelength has a finite shift with the changing of $\alpha$, the amplitude of $r_{LL}$ can be continuous manipulated at a fixed wavelength (the operation wavelength for $\alpha$ equal to 45 degrees), as shown in Figure 4c. According to the quantitative analysis in Figure S4i–p, the strength of the resonance induced by the antiparallel currents within the nanostructures can be directly manipulated by changing angle $\alpha$, resulting in the spin-selective amplitude manipulation of optical waves with a large modulation depth.

Moreover, for nanoantennas with structural symmetry breaking, the second-order resonance can be excited when the equivalent wavelength of optical waves equals to the length $L$ of the nanoantenna, which means that the operation wavelength of the nanoantenna is proportional to its length. In a similar way, the operation wavelength of the proposed chiral mirror is proportional to the sum of the length of the long arc and the horizontal nanorod. Thus, we can manipulate the operation wavelength by changing the length of the long arc (angle $\beta$). To quantitative reveal the relationship between the angle $\beta$ and the optical response of the chiral mirrors, we analyzed the optical responses of the enantiomorph A with different structural variable $\beta$, as shown in **Figure S5**. According to the simulated results in Figure S5e–h, the operation wavelength can be effectively manipulated while the performance of the spin-selective reflection remains unchanged, and the variation of operation wavelength is almost proportional to the variation of $\beta$. Moreover, from the quantitative analysis in Figure S5i–p, we can further confirm that the excitation of multipolar resonance within the designed chiral mirror remains unchanged. It is worth mentioning that the results in Figure S5i–p show that the scattering intensity of each component decrease with the red-shift of the operation wavelength, which does not mean that the resonance strength of each component decrease with the red shift of the operation wavelength, because the scattering intensity is inversely proportional to the wavelength. Actually, according to the qualitative analysis in Figure S5a–d, the resonance strength is similar at the operation wavelength for enantiomorph A with different angle $\beta$. As we mentioned in section 2, the variation of $r_2$ results in a larger shift of the operation wavelength when compared with other structural parameters, especially $r_1$. That because the length of the long arc (approximate to $\beta(r_1+r_2)$) and the length of the horizontal nanorod (approximate to $2r_2$) are both changed with the variation of $r_2$, while only the length of the long arc is changed with the variation of $r_1$. Also, we can obtain that the finite variation of the structural parameter $P$ (period along $x$ and $y$ axis) and $w$ (the width of the horizontal nanorod) have limited affection on the optical response of the designed chiral mirror, because

both the length of the long arc and the length of the horizontal nanorod are not changed accordingly. Furthermore, the variation of angle $\alpha$ will induced a finite shift of the operation wavelength because it has a limited affection on the equivalent length $L$. To sum up, the operation wavelength can be continuous manipulated in a broad bandwidth with the designed chiral mirrors by adjusting the angle $\beta$, as shown in Figure 4f.

According to the results in Figure 2, the designed chiral mirrors can not only realize the spin-selective reflection of optical waves, but also change their spins ($r_{LL}$ or $r_{RR}$ are not equal to zero while $r_{LR}$ and $r_{RL}$ are equal to zero). Thus, we can realize the 0 to $2\pi$ phase manipulation of optical waves by utilizing the geometric phase: when a circular-polarized optical wave reflected by a nanostructure with a rotation angle of $\varphi$, it will add an extra phase of $\pm 2\varphi$ to the reflected wave with opposite spin. By changing the orientation angle $\theta$ from 0 to $\pi$, we can manipulate the phase of the reflected waves from 0 to $2\pi$, as shown in Figure 4i. To further validate the phase manipulation of optical waves in the designed chiral mirrors, we designed two gradient metasurfaces composed of rotated chiral mirrors with opposite optical responses, as shown in **Figure S6**a,b. According to the simulated results in Figure S6c,f, the proposed gradient metasurfaces in Figure S6a can realize the anomalous reflection of RCP waves at the operation wavelength, while the anomalous reflection of both LCP and RCP waves can be realized at the wavelength away from the operation wavelength (Figure S6d,g). On the contrary, the proposed gradient metasurfaces in Figure S6b can realize the anomalous reflection of LCP waves at the operation wavelength (Figure S6e,h). These results validate that the phase of the reflected waves can be well manipulated by the proposed chiral mirrors.
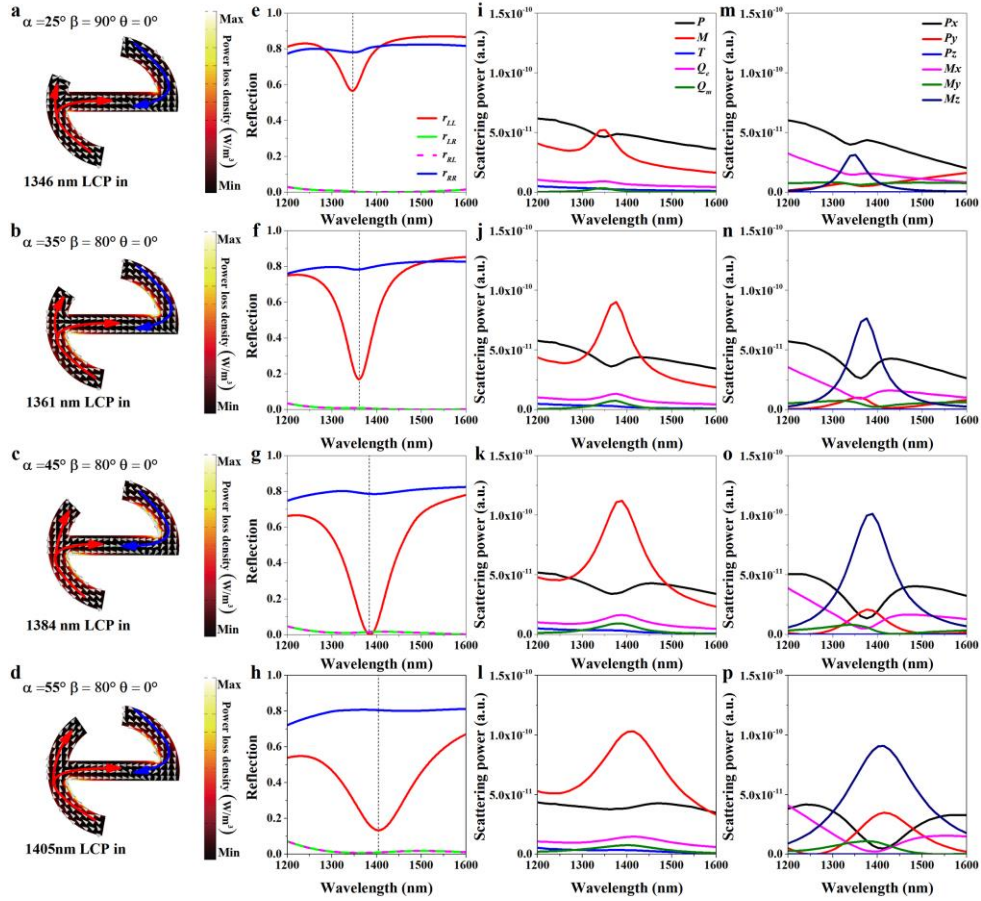
**Figure S4.** The analysis on the physical mechanisms for the spin-selective amplitude manipulation with the designed chiral mirrors. The results in each line corresponds to an enantiomorph A with a different structural variable α. (a)-(d) Simulated results of the direction of the current flow (white arrow) and the distribution of power loss density in the enantiomorph A (on the middle section of the nanostructure in a unit cell) with LCP illumination and with structural variables β equals to 80 degrees and θ equals to 0 degree: (a) at 1346 nm (The black dotted line in Figure S3(e)) with structural variable α equals to 25 degrees; (b) at 1361 nm (The black dotted line in Figure S3(f)) with structural variable α equals to 35 degrees; (c) at 1384 nm (The black dotted line in Figure S3(g)) with structural variable α equals to 45 degrees. (d) at 1405 nm (The black dotted line in Figure S3(h)) with structural variable α equals to 55 degrees. (e)-(h) Simulated modular square of the reflection coefficients for the enantiomorph A in (a)-(d). (i)-(p) Calculated multipolar decomposition of scattering spectra of the enantiomorph A in (a)-(d) in terms of electric dipole (P), magnetic dipole (M), toroidal dipole (T), electric quadrupole ($Q_e$), magnetic quadrupole ($Q_m$) and the component of electric dipole (P) and magnetic dipole (M) with LCP illumination.
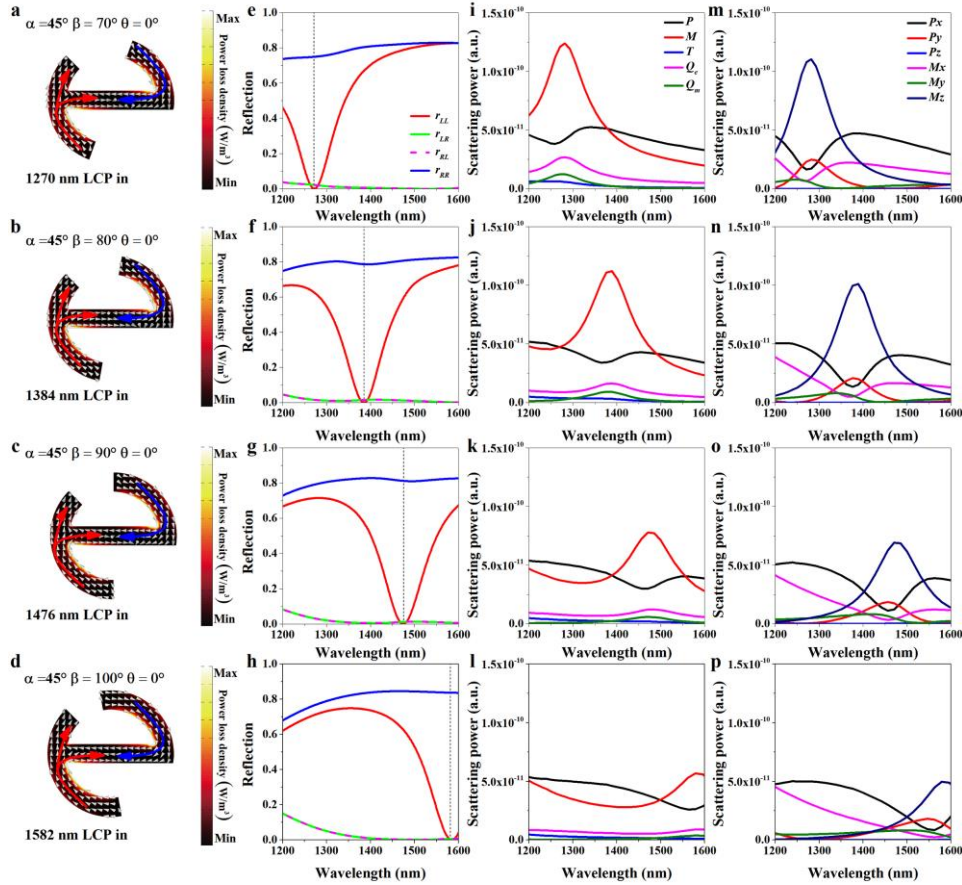
**Figure S5.** The analysis on the physical mechanisms for the wavelength-selective amplitude manipulation with the designed chiral mirrors. The results in each line corresponds to an enantiomorph A with a different structural variable β. (a)-(d) Simulated results of the direction of the current flow (white arrow) and the distribution of power loss density in the enantiomorph A (on the middle section of the nanostructure in a unit cell) with LCP illumination and with structural variables α equals to 45 degrees and $\theta$ equals to 0 degree: (a) at 1270 nm (The black dotted line in Figure S4(e)) with structural variable β equals to 70 degrees; (b) at 1384 nm (The black dotted line in Figure S4(f)) with structural variable β equals to 80 degrees; (c) at 1476 nm (The black dotted line in Figure S4(g)) with structural variable β equals to 90 degrees. (d) at 1582 nm (The black dotted line in Figure S4(h)) with structural variable β equals to 100 degrees. (e)-(h) Simulated modular square of the reflection coefficients for the enantiomorph A in (a)-(d). (i)-(p) Calculated multipolar decomposition of scattering spectra of the enantiomorph A in (a)-(d) in terms of electric dipole (P), magnetic dipole (M), toroidal dipole (T), electric quadrupole ($Q_e$), magnetic quadrupole ($Q_m$) and the component of electric dipole (P) and magnetic dipole (M) with LCP illumination.
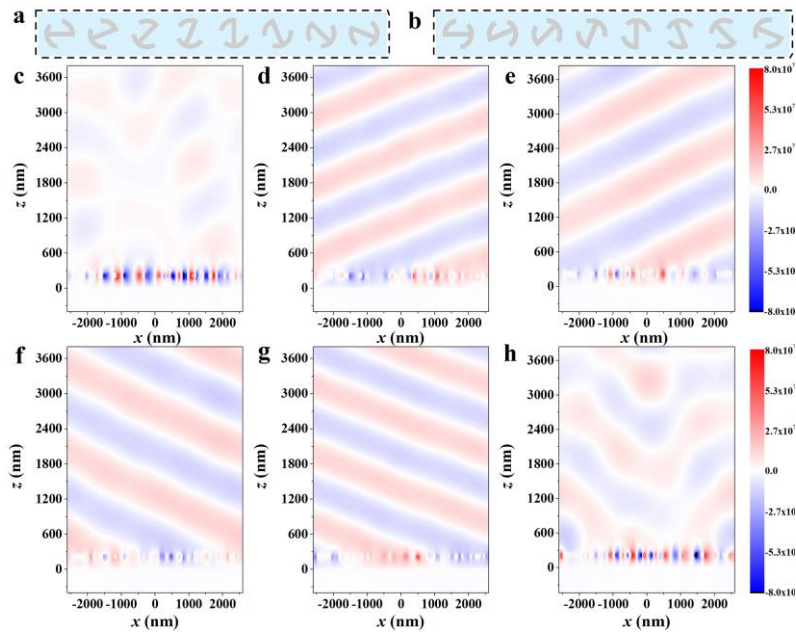
**Figure S6.** Spin-selective anomalous wave generation with the designed gradient chiral mirrors. (a) Schematic of the gradient chiral mirror composed of enantiomorph A with different structural variable $\theta$ ($\Delta\theta=\pi/8$) for spin-selective generation of RCP anomalous wave. (b) Schematic of the gradient chiral mirror composed of enantiomorph B with different structural variable $\theta$ for spin-selective generation of LCP anomalous wave. (c),(d),(f),(g) The electric field distributions in $x$-$z$ plane for design in Figure S5a and (e),(h) the electric field distributions in $x$-$z$ plane for design in Figure S5b under normal illumination of (c)-(e) LCP and (f)-(h) RCP optical waves at (c),(f) 1408 nm (working wavelength), (d),(g) 1150 nm and (e),(h) 1408 nm respectively.

**Section 5. Design principle of the spin- and wavelength encoded imaging with the designed chiral mirrors**

Four basic unit cells are proposed to realize the 2-bit spin-encoded imaging with dual outputs, as shown in **Figure S7**a. #2 and #3 are enantiomorph A and B, respectively. #1 is obtained from #2 by deleting the aluminum nanostructure on the top layer, and #4 is obtained from #2 by deleting the short arc part of the nanostructure. To validate the optical response of these four basic unit cells, we simulated the modular square of their reflection coefficients as shown in Figure S7b. The simulated results indicate that the optical response of #1 is as same as a normal mirror without spin conversion and the optical response of #4 is as same as a handedness-preserving mirror in a broad bandwidth, while #2 and #3 are chiral mirrors with opposite spin-selective reflections around 1384 nm. By utilizing these four basic unit cells, we can realize spin-selective 2-bit reflection intensity encoding, as shown in Figure S7c. For LCP illumination with LCP detection ("LCP/LCP"), the reflection intensities of #1 and #2 are close to zero around 1384 nm while them of #3 and #4 are over 0.8. For RCP illumination with RCP detection ("RCP/RCP"), the reflection intensities of #1 and #3 are close to zero around 1384 nm while them of #2 and #4 are over 0.8. Thus, under these two illumination and detection conditions, the four basic units can be treated as coding unit "00", "01", "10" and "11", respectively. Figure S7d shows the experimental results of the designed spin-encoded QR code in Figure 5a under broadband illumination, it is clear that the QR code cannot be observed even under specific illumination and detection state. Thus, spin-encoded imaging based on the proposed chiral mirrors is a good alternative for optical encryption.

Another two basic unit cells are proposed to replace #2 and #3 to further realize the 2-bit spin- and wavelength-encoded imaging with dual outputs, as shown in **Figure S8**a. #5 and #6 are enantiomorph A with structural variable $\beta = 68$ degrees and $\beta = 85$ degrees, respectively. Simulated results of the modular square of their reflection coefficients are shown in Figure S8b, which indicate that #5 and #6 are chiral mirrors with same spin-selective reflection

around two different wavelengths. By utilizing these four basic unit cells, we can realize spin-and wavelength-selective 2-bit reflection intensity encoding, as shown in Figure S8c. For LCP illumination with LCP detection, the reflection intensities of #1 and #5 are close to zero around 1252 nm while them of #4 and #6 are over 0.6. At the same time, the reflection intensities of #1 and #6 are close to zero around 1422 nm while them of #4 and #5 are over 0.7. Thus, under LCP illumination with LCP detection at these two different wavelengths, the four basic units can be treated as coding unit "00", "01", "10" and "11", respectively.
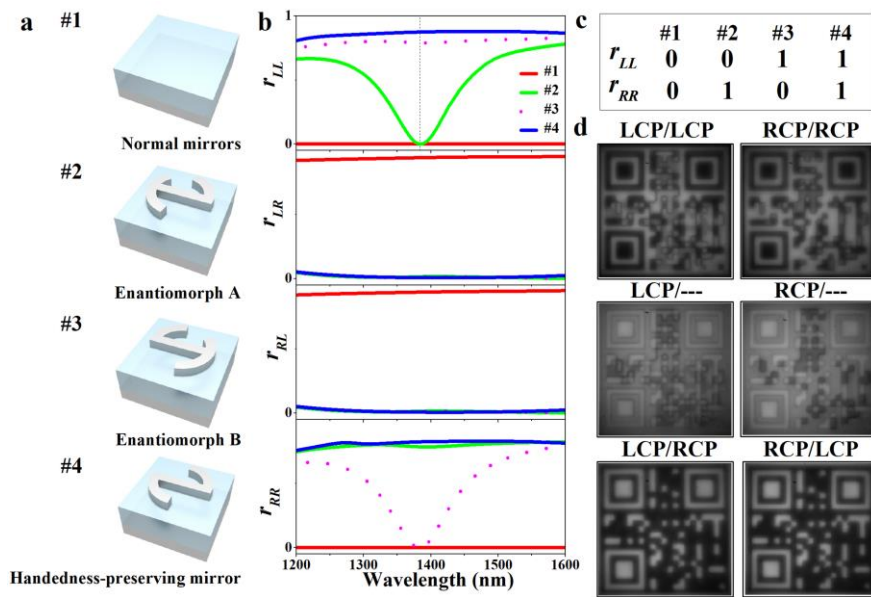


**Figure S7.** Schematic of the spin-encoded imaging with the designed chiral mirrors. (a) Schematic of four basic unit cells for the implementation of spin-encoded imaging with dual outputs. (b) Simulated results of the modular square of the reflection coefficients for the four basic unit cells. (c) Schematic of the 2-bits spin-encoded imaging with the design four basic unit cells around 1384 nm (The black dotted line in Figure 6(b)). (d) Experimental results of the spin-encoded QR code under broadband illumination (under the illumination of a bromine tungsten lamp without wavelength filter) with different illumination and detection states respectively.
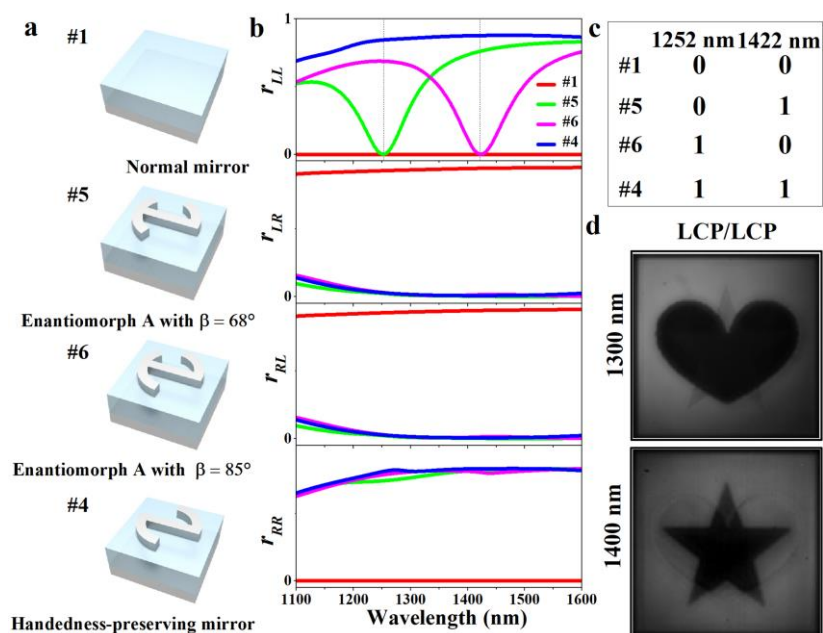
**Figure S8.** Schematic of the spin- and wavelength-encoded imaging with the designed chiral mirrors. (a) Schematic of four basic unit cell for the implementation of wavelength-encoded imaging with dual outputs. (b) Simulated results of the modular square of the reflection coefficients for the four basic unit cells. The black dotted line shows the position of 1252 nm and 1422 nm. (c) Schematic of the 2-bits spin- and wavelength-encoded imaging with the designed four basic unit cells under LCP illumination and detection. (d) Experimental results of the spin- and wavelength-encoded imaging with LCP illumination and detection at 1300 nm and 1400 nm, respectively. The image was captured under the illumination of a bromine tungsten lamp with wavelength filters.

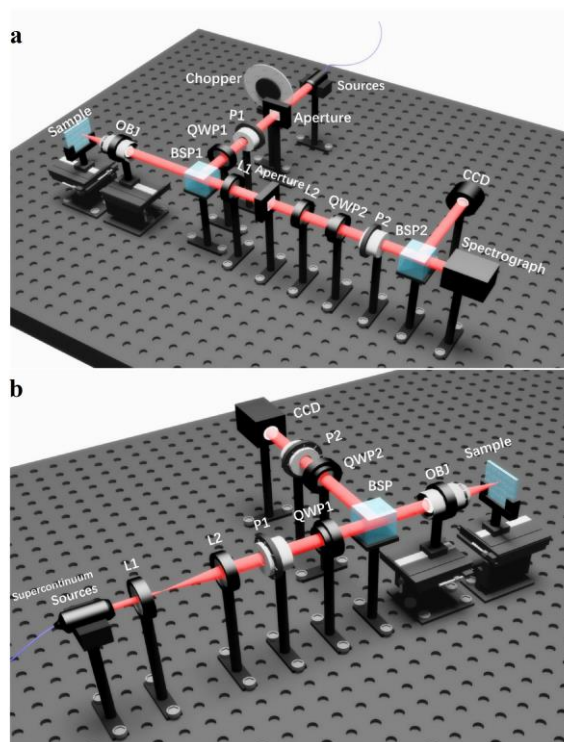**Section 6. The experimental setup for spectra measurement and optical imaging**



**Figure S9.** The experimental setup for spectra measurement and optical imaging. (a) The experimental setup for spectrum measurement and imaging with bromine tungsten lamp and filter plate. (b) The experimental setup for imaging with supercontinuous laser. L: lens, P: Polarizer, QWP: quarter-wave plate, OBJ: objective, BSP: beam splitter prism.